



Classifying transformation-variant attributed point patterns

K.E. Dungan*, L.C. Potter

Department of Electrical and Computer Engineering, The Ohio State University, 2015 Neil Ave, Columbus, OH, USA

ARTICLE INFO

Article history:

Received 27 August 2009

Received in revised form

25 May 2010

Accepted 28 May 2010

Keywords:

Point pattern matching

Hausdorff distance

SAR

Multidimensional scaling

Fingerprint

ABSTRACT

This paper presents a classification approach, where a sample is represented by a set of feature vectors called an attributed point pattern. Some attributes of a point are transformational-variant, such as spatial location, while others convey some descriptive feature, such as intensity. The proposed algorithm determines a distance between point patterns by minimizing a Hausdorff-based distance over a set of transformations using a particle swarm optimization. When multiple training samples are available for each class, we implement multidimensional scaling to represent the point patterns in a low-dimensional Euclidean space for visualization and analysis. Results are demonstrated for latent fingerprints from tenprint data and civilian vehicles from circular synthetic aperture radar imagery.

© 2010 Elsevier Ltd. All rights reserved.

1. Introduction

Suppose that a class sample is represented by a collection of feature vectors consisting of transformation-variant features along with other attributes. For example, a fingerprint can be represented by a set of minutiae, each containing two-dimensional (2D) spatial location along with type and orientation attributes [1]. The collection of feature vectors is referred to as an attributed point pattern or point set. The locations are subject to an unknown rigid transformation. When comparing two different samples, it may be necessary to register the location information before comparing the two point sets.

Researchers have approached point set classification by adopting a data representation that is invariant to a class of transformations. Example methods include graph based methods [2] and spectral correspondence methods that compare the point adjacency matrices from patterns [3,4]. Typically, the transformation invariant approaches yield matching performances that break down in the presence of noise, clutter, and occlusion [5].

Other researchers have developed methods to directly register two sets. Early methods [6,7] require a correspondence and minimize the sum of squared distances between corresponding points. Later methods iteratively discover a correspondence during the registration process with the iterative closest point (ICP) method [8,9]. To remove the correspondence all together, some have applied Hausdorff distance based registration [10,11] or a difference of convex functions formulation [12].

In this paper we estimate the registration of sets using a Hausdorff distance based technique. Registration and set distance are related; the estimated registration between two sets yields the minimum distance between the two sets. Thus we refer to the distance between two sets under their estimated registration simply as the set distance (SD). Partial versions of the Hausdorff distance [10,13,14] are naturally robust to clutter and occlusions since they find a best subset match between two sets.

In previous work, Yin [11] demonstrated a method to register two 2D point patterns by minimizing a partial Hausdorff distance between the two patterns with a particle swarm optimization. The Yin article registered synthetically generated 2D point patterns perturbed by rigid transformations, random clutter, and random occlusions. We extend Yin's contribution with four meaningful steps:

- In addition to 2D location, we include attributes that add more information to the point pattern. The associated distance between individual points can be characterized with a Mahalanobis distance using an appropriately selected error covariance matrix.
- In addition to registering point patterns, we use a version of the minimized partial Hausdorff distance as a pseudo-metric for a nearest neighbor (NN) classifier. Augmented distance matrices created from multiple samples are observed to be nearly positive definite, which reveals that the pseudo-metric well approximates a valid distance measure.
- We demonstrate the first classification results for persistent radar surveillance; prior art has been restricted to narrow apertures. Further, we give the first published results for classification of civilian sedans, which present very small and

* Corresponding author.

E-mail address: dungank@ece.osu.edu (K.E. Dungan).

very similar radar signatures, in comparison to military vehicles. To illustrate the generic applicability of attributed point patterns, we also present a small example for latent fingerprints.

- For applications with multiple training samples, we describe multidimensional scaling (MDS) and Landmark MDS (LMDS) as tools for visualization, analysis, and alternative classifiers.

Advances in processing and high performance computing have made it possible to tractably solve optimizations necessary for the registration and classification in a multiclass problem [15,16]. Fig. 1 describes the proposed classification algorithm. Given a database of training images, we extract a set of transformation-variant feature vectors (attributed points) for each image; the database is represented as a set of sets $H = \{H_1, H_2, \dots, H_n, \dots\}$. Then, given a query image, we extract a set Q of attributed points and calculate a set distance d_i from the query to each set in the database. Using a nearest neighbor test, the classification C is determined from the minimum set distance between Q and each H_i . Thus,

$$C = \arg \min_i d(Q, H_i). \quad (1)$$

Fig. 1 shows several application specific parameters used in the set distance calculation. The distances between attributed point patterns are minimized under a transformation T . The measurement error covariance matrix Σ is used to calculate a Mahalanobis distance between individual feature vectors. Based on the estimated level of clutter in a query, the parameter K is set to facilitate the best subset match. Finally, the particle swarm optimization (PSO) is run for a specified number of particles and iterations as determined by training.

Notice that green boxes in Fig. 1 are performed offline, while dashed boxes are part of the optional MDS/LMDS chain. If multiple training samples are available, it is possible to generate a matrix of distances d_{ij} between patterns in the union of classes. By applying multidimensional scaling (MDS), the samples are represented in a Euclidean space, $X_i \in \mathbb{R}^n$, for a visualization of class separation and an analysis of the pseudo-metric. Given the points in the Euclidean space, it is possible to train classifiers other than NN, such as a support vector machine (SVM) or a linear discriminant analysis (LDA) classifier. When a measured query sample Q is available, we can map the sample into the Euclidean space using a landmark MDS algorithm (LMDS) [17] for visualization or classification.

The remaining sections are organized as follows. Section 2 describes Fig. 1 with subsections detailing the set distance, MDS analysis/training, and LMDS visualization/classification. In Section 3 we use the proposed approach in two applications: latent fingerprint classification and 10-class vehicle classification using circular synthetic aperture radar (SAR). Section 4 provides a summary and discussion of results.

2. Set classification

2.1. Sets distances using the Hausdorff distance

The Hausdorff distance (HD) is a well-known method for representing the distance between two point sets without having a prior correspondence between the two sets. Huttenlocher et al. [10] applied the classical Hausdorff measure [18] concept to matching point sets. Essentially, the HD is the distance of the most isolated point between Q and H_i . However, an outlier or occlusion could skew an otherwise close registration, in which case, the partial Hausdorff distance (PHD) [10], which is the K th minimum distance between points in the sets, may be used. We apply a more robust form of the PHD called the least trimmed square Hausdorff distance (LTS-HD), which takes the mean of the K minimum distances between point sets [19]. To formally describe the LTS-HD, first let $d_{H_i}(\mathbf{q})$ be the distance from any $\mathbf{q} \in Q$ to its nearest neighbor in H_i , and let $d_{H_i}(\mathbf{q})_{(k)}$ denote the k th value from the sorted sequence of nearest neighbor distances calculated for all members of Q to H_i . The directed LTS-HD may be written

$$h_K(Q, H_i) = \frac{1}{K} \sum_{k=1}^K d_{H_i}(\mathbf{q})_{(k)}. \quad (2)$$

The point sets Q and H_i are not necessarily registered prior to calculating the LTS-HD. Rucklidge [20] investigated minimizing the PHD over rigid transformations with scaling. We build upon this concept by using the LTS-HD and generalizing the underlying norm with the Mahalanobis distance [21]. The resulting set distance is defined by

$$d_i = \min_T h_K(T(Q), H_i), \quad (3)$$

where T is the set transformation. In our application, T defines rigid transformations in a 2D plane; however, T is flexible to fit the desired application such as scaling, shifts in time, or 3D transformations.

The underlying nearest neighbor distances in (2) are calculated from the Mahalanobis distance, here represented as a norm between $\mathbf{q} \in Q$ and $\mathbf{h} \in H_i$ such that

$$\|\mathbf{q} - \mathbf{h}\| = \sqrt{(\mathbf{q} - \mathbf{h})^T \Sigma^{-1} (\mathbf{q} - \mathbf{h})}, \quad (4)$$

where Σ is the measurement error covariance matrix for the vectors in a point set. The Mahalanobis distance facilitates the comparison of vectors, where the various dimensions have different scales, different error sources, or correlated errors. For example, in radar, some attributes may contain spatial locations of bright reflectors, while other attributes contain information about intensity, polarization, or direction of illumination. Use of an appropriate error covariance matrix increases class separability. In practice, it is typical to estimate the measurement error variances of each feature in the feature vectors to populate the diagonal of Σ ; however, determining the off-diagonal covariance terms may improve results.

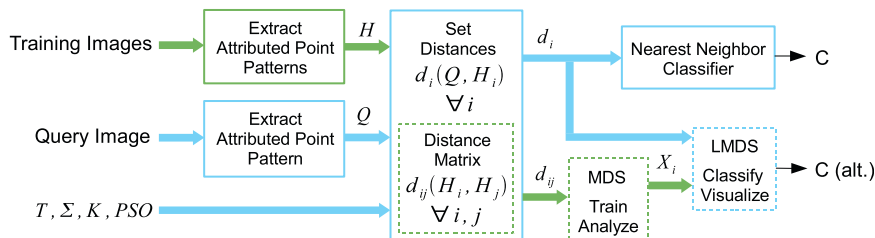


Fig. 1. Calculate the set distance between the query Q and each class sample H_i ; the nearest neighbor classification is the shortest distance. An optional chain of processing for analysis/visualization or alternative classifiers using MDS/LMDS is indicated with the dashed boxes. Offline processing is shown in green. (For interpretation of the references to color in this figure legend, the reader is referred to the web version of this article.)

Mount et al. [22] suggest setting K in (2) as a fraction of the cardinality of one of the sets; thus in our application,

$$K = \lfloor r \min\{|Q|, |H_i|\} \rfloor, \quad 0 < r \leq 1. \quad (5)$$

For example, a value of $r=0.6$ would mean d_i is minimized over a subset of 60% of the points in Q , supposing $|Q| < |H_i|$. Hence, the pattern match would be immune to a number of spurious or occluded points. In applications, the designer should estimate the average clutter ratio in query data and set r a little lower.

To calculate the set distance of (3), we minimize the LTS-HD over the set of allowable transformations using a nonconvex technique called a particle swarm optimization (PSO). The PSO as a generic nonconvex optimization tool is explored in detail by Clerc and Kennedy [23], with emphasis on convergence to local versus global minima. In a precursor to our application, Yin [11] applies a PSO to find the global minimum PHD over rigid transformations with scaling between two 2D point sets. To search the 2D affine space with scaling, the set transformation is defined by

$$T(\mathbf{q}) = sR\mathbf{q} + \mathbf{t} \quad \forall \mathbf{q} \in Q. \quad (6)$$

Thus, the PSO searches for an angle in the rotation matrix R , a scaling factor s , and a translation vector $\mathbf{t} = (t_x, t_y)^T$ for an optimization over four variables. Due to the physics of our applications, we do not allow scaling.

The PSO algorithm requires initializing a number of particles (i.e. t_x and t_y translations and ψ rotation) and running the algorithm for a number of iterations; the initializations are randomly set within application-specific bounds. The particles then move as the PSO algorithm converges to a local minimum [23,11]. As with any nonconvex optimization problem, it is possible to converge upon a local minimum that is not the global minimum. In general, more particles and iterations implies a greater chance of finding the global minimum at the expense of processing those extra particles. Efficient selection of stopping criteria for PSO is an open problem explored by Kwok et al. [24]. However, a sufficient number of particles and iterations can be empirically set using training data.

When minimizing an LTS-HD over a set of transformations, it is possible to find the same point pattern in multiple places within the same point set. Hence, the resulting set distance could violate the metric properties of nondegeneracy and triangle inequality; the directed LTS-HD may fail under symmetry as well. However, as the diversity of information and point set sizes increase, it is less likely to find repeated patterns leading to metric violations. The next section describes multidimensional scaling as applied to set distances, and the eigenvalues that are generated offer evidence to the suitability of the set distance as a metric. Use of the pseudo metric is further justified by strong classification performance in practice.

In summary, the set distance (3) requires setting T , K , Σ , and the PSO parameters; all of these are deterministic for the desired application. The set distance design is robust to an unlimited number of applications, and for two of these, fingerprints and SAR, we demonstrate specific design decisions for the four parameters.

2.2. MDS for analysis and/or training

Because a sample is defined as an unordered set of transformation-variant vectors, it cannot be plotted as a single point in an inner product space. Furthermore, it is not possible to visualize a comparison of point patterns since they do not exist in a Euclidean space. However, given a collection of samples and a matrix of set distances between those samples, it is possible to approximately represent the collection of samples in a Euclidean space using multidimensional scaling (MDS). The representation

of point patterns as a single point in a low-dimensional Euclidean space permits visualization of data and allows for the use of classifiers other than NN. Additionally, for analysis purposes, the eigenvalues generated during the MDS process provide evidence showing how close the pseudo-metric is to a true metric.

We apply MDS as described by Potter and Chiang [25]; given a set of samples, a Euclidean distance matrix (EDM) stores all pairwise distances between samples. If the distance measure follows the rules of a metric space, then the EDM is symmetric with zeros on the diagonal. By squaring the distances in the EDM, we define an m -by- m matrix D . Schoenberg [26] proved the following theorem:

Theorem 1. Let $\mathbf{e} \in \mathbb{R}^m$ be given by $\mathbf{e} = [1, 1, \dots, 1]^T$, and let Φ be the orthogonal projection matrix onto the subspace $M = \{\mathbf{x} \in \mathbb{R}^m : \mathbf{x}^T \mathbf{e} = 0\}$, i.e.,

$$\Phi = I - \frac{1}{n} \mathbf{e} \mathbf{e}^T. \quad (7)$$

A matrix D has representation by pairwise distances of m points in \mathbb{R}^{m-1} if and only if $\Phi D \Phi^T$ is a positive-semidefinite matrix. Further, for the matrix D to admit representation in the embedding space \mathbb{R}^n for $n < m-1$ requires $\text{rank}(\Phi D \Phi^T) \leq n$.

Finally, we solve the eigendecomposition $\Phi D \Phi^T = U \Lambda U^T$, and the rows of $U \Lambda^{1/2}$ are the Euclidean embedding of the point set into an n -dimensional space.

Suppose that we have multiple samples for two different classes H_{i*} and H_{j*} where “*” represents a wildcard for all of the samples within a given class. First, we construct a matrix of squared distances between each sample. For example, with four training samples from two classes, $\Psi_{ij} = \{H_{i1}, H_{i2}, H_{j1}, H_{j2}\}$, we generate a matrix of squared set distances with zeros on the diagonal

$$D_{ij} = \begin{bmatrix} 0 & d_{12}^2 & d_{13}^2 & d_{14}^2 \\ d_{12}^2 & 0 & d_{23}^2 & d_{24}^2 \\ d_{13}^2 & d_{23}^2 & 0 & d_{34}^2 \\ d_{14}^2 & d_{24}^2 & d_{34}^2 & 0 \end{bmatrix}. \quad (8)$$

The subscripts of the matrix entries correspond to the position in Ψ_{ij} ; for example,

$$d_{13} = \min_T h_K(T(H_{i1}), H_{j1}). \quad (9)$$

If $|\Psi_{ij}| = m$, then calculating D_{ij} requires $m(m-1)/2$ distance calculations. Upon eigendecomposition of

$$\Phi D_{ij} \Phi^T = U_{ij} \Lambda_{ij} U_{ij}^T, \quad (10)$$

we find the embedding

$$X_{ij} = \Lambda_{ij}^{1/2} U_{ij}^T \quad (11)$$

and design a classifier to choose between the classes i and j . With the eigenvalues in Λ_{ij} in descending order from maximum magnitude, truncating the first n columns of X_{ij} provides an embedding in \mathbb{R}^n .

If our defined set distance (i.e. minimized LTS-HD) were a proper metric, then $\Phi D \Phi^T$ would always be positive-semidefinite. However, noisy measurements, occasional violation of the triangle inequality, or occasional failure to find a global minimum in (3) will cause some negative eigenvalues. Qualitatively, a few small negative eigenvalues relative to several large positive eigenvalues lends evidence that the pseudo-metric may be useful in the application.

2.3. LMDS for visualization and/or classification

As described in Section 2.2, a collection of training samples $H_i \in H$ can be embedded in a low-dimensional Euclidean space for analysis. Given a new query Q , it is possible to add a row and column to the matrix D_{ij} with distance measurements to the new sample Q and apply MDS to embed the measurement,

$$\{H_{i_1}, H_{i_2}, \dots, H_{j_1}, H_{j_2}, \dots, Q\} \xrightarrow{\text{MDS}} \quad (12)$$

$$\{h_{i_1}, h_{i_2}, \dots, h_{j_1}, h_{j_2}, \dots, q\} \subset \mathbb{R}^n. \quad (13)$$

Then, with the training samples in $\{h_{i_1}, h_{i_2}, \dots, h_{j_1}, h_{j_2}\} \subset \mathbb{R}^n$, one could design a classifier and classify q .

However, each new query would require a new embedding and new training. Furthermore, to visualize multiple queries in the same Euclidean embedding would require expanding the EDM with extra rows and columns for the additional queries along with the distances between the queries themselves. Fortunately, a technique called landmark MDS (LMDS) [17] provides a method to add query samples to a Euclidean space based on distances to training samples that were previously embedded using MDS. Thus all training and query samples can be visualized together, and a classifier need be trained only once. Using a common embedding, however, may cause a suboptimal embedding for individual measurements.

To implement LMDS, Silva [17] describes a method to invert the eigendecomposition of the embedding and apply the result to the landmarks. Let X_t be the pseudo-inverse $(A_{ij}^{1/2} U_{ij}^T)^+$ truncated to the dominant n eigenvalues (i.e. the embedded dimension). Thus, adding a new measurement x_q to an existing embedding of the training samples is

$$x_q = -\frac{1}{2} X_t (\delta_q - \delta_\mu), \quad (14)$$

where δ_q is the vector of squared distances to the landmarks and δ_μ is the mean vector of squared distances from each landmark to all of the other landmarks.

To implement a multiclass classifier using MDS/LMDS in our SAR example, we chose to use a binary decision tree. During offline training, we apply MDS to the N choose two pairings of the training classes. Then, in the decision process, we apply LMDS to add the query samples to the low-dimension embeddings. For M classes, the decision tree requires $M-1$ binary decisions.

3. Applications

3.1. Latent fingerprints

Fingerprints of varying quality that are incidentally left and extracted from a scene are referred to as latent, while a tenprint refers to fingerprints that are collected and recorded in a controlled setting onto fingerprint cards [27]. In this section, we apply set distances to classify latent fingerprints to a database of tenprints.

3.1.1. Classifying latent fingerprints

The National Institute of Standards and Technology (NIST) special database 27 (SD27) contains 258 latent fingerprint images, which are subdivided into 88 good, 85 bad, and 85 ugly images [27]. SD27 also contains 258 tenprint images corresponding to the latent images. It is common to extract key points on a fingerprint such as ridge endings or bifurcations that are collectively called fingerprint minutiae. For both the latent and tenprint images, SD27 provides sets of minutiae with location, orientation, type, and quality attributes. Minutiae in the latent fingerprints of SD27

typically represent a small subset of the minutiae in the tenprint. Some of the latent fingerprints have fewer than 10 minutiae, while the tenprint images typically have on the order of 100 minutiae.

We independently classified each set of latent minutiae to the 258 tenprint classes using the NN classifier path of Fig. 1, where Fig. 2 summarizes the registration and set distance process in comparing a latent image to a tenprint. Fig. 2(a) offers an example latent fingerprint image with minutiae locations indicated by blue circles, where the small line in each blue circle indicates the direction of the minutiae orientation attribute. Next, the image in Fig. 2(b) shows the corresponding tenprint image with minutiae shown in red. By minimizing the Hausdorff distance over T as in (3), Fig. 2(c) and (d) show the latent minutiae in blue registered to the tenprint minutiae in red. In (c), the view of the x and y location attributes easily relates back to the minutiae in (a) and (b), while the plot in (d) provides a visualization of the orientation attribute on the z -axis. The orientation attribute increases the diversity of information, making it less likely to find the same point pattern in a different part of the tenprint.

3.1.2. Feature vector and covariance

The minutiae type and quality attributes are undetermined for the tenprint database entries of SD27. Thus, we consider only the location and orientation attributes of the minutiae, and the transformation in calculating the set distance is given by

$$T_i \begin{pmatrix} q_{ix} \\ q_{iy} \\ q_{i\theta} \end{pmatrix} = \begin{bmatrix} \cos\psi & -\sin\psi \\ \sin\psi & \cos\psi \\ \text{mod}(q_{i\theta} + \psi, 2\pi) \end{bmatrix} \begin{bmatrix} q_{ix} \\ q_{iy} \end{bmatrix} + \begin{bmatrix} t_x \\ t_y \end{bmatrix}. \quad (15)$$

In calculating the LTS-HD of (2), the norm is calculated as a Mahalanobis distance in (4). To select the covariance matrix Σ of measurement errors, we populated the diagonal elements with location variances σ_x^2 and σ_y^2 and orientation variance σ_θ^2 . We first selected variances based on an estimate, then trained on three latent/tenprint pairs to maximize the inter class separations in the LTS-HD. To start, we assumed 95% confidence that the location information is within two pixels of the true locations. Thus,

$$2 = 1.98\sigma_x \Rightarrow \sigma_x^2 = \sigma_y^2 = 1, \quad (16)$$

where 1.98 is the z -score associated with 95% of the area under a normal distribution. Using the same logic, we assumed that the orientation attribute is measured accurately within 5° with 95% confidence. Thus,

$$5 = 1.98\sigma_\theta \Rightarrow \sigma_\theta^2 = 2.5. \quad (17)$$

After training on the three pairs, we determined that these initial estimates worked well.

Next, defining the LTS-HD requires setting K using r in (5). Intuitively, a smaller K increases the chance of finding multiple pattern matches in the tenprint images (i.e. $K=1$ would allow a zero set distance at every point in the tenprint). By increasing K , it is less likely to violate the nondegeneracy property of distances. However, if K is too large, then false minutiae are matched to the tenprint. Based on training with three images (identical to that used for determining Σ), we set $r=0.75$ to ignore a quarter of the latent minutiae.

3.1.3. Latent fingerprint classification results

Classification results are displayed in Fig. 3, which displays the probability that the correct tenprint appears among the $N=\text{rank}$ minimum set distances. For example, a P_{id} with rank 10 means that an image is correctly classified in the top 10 selections with a probability P_{id} . Results are displayed for good, bad, and ugly images, where rank-1 P_{id} is 0.89, 0.64, and 0.60, respectively. The

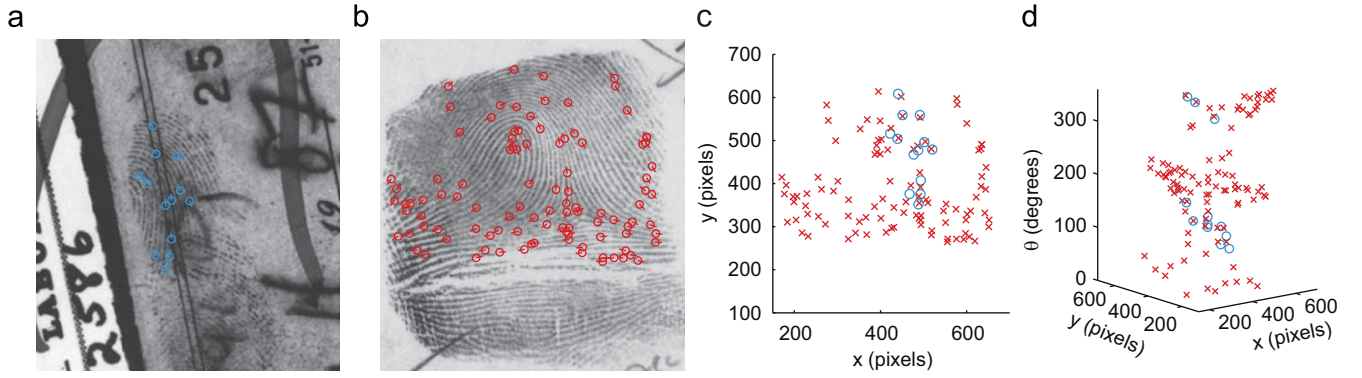


Fig. 2. The image in (a) is a latent fingerprint with overlaid minutiae, and (b) is a tenprint image with overlaid minutiae. The plot in (c) shows the registration of the latent and tenprint location information, while (d) adds the orientation field information.

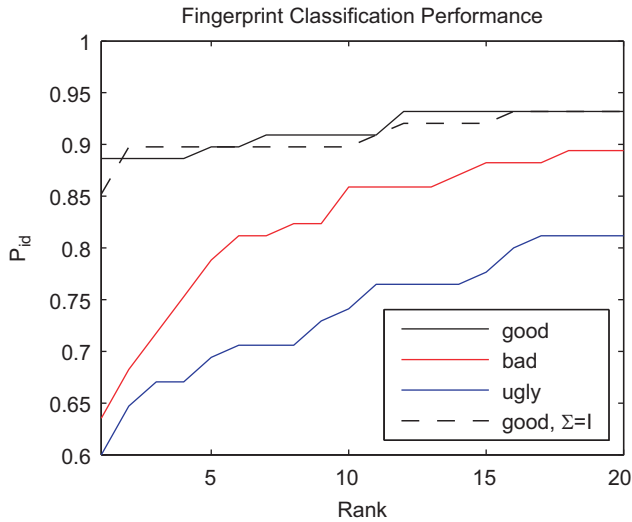


Fig. 3. Higher quality latent imagery results in higher probability of identification. The black line shows that good latent images are identified in the top five or so tenprint images around 90% of the time. Bad images are shown in red with ugly in blue. (For interpretation of the references to color in this figure legend, the reader is referred to the web version of this article.)

rank-20 accuracy is 0.93, 0.89, and 0.81. When combining all three image types, the rank-1 $P_{id}=0.71$ and the Rank-20 $P_{id}=0.88$.

To demonstrate the effect of the measurement error covariance matrix Σ , we classified the good latent fingerprint data using a unity covariance matrix. The effect of changing σ_θ^2 from 2.5 to 1 is to add more importance to the minutiae orientation attribute since Σ is inverted in the Mahalanobis distance. As shown in Fig. 3 with the black dashed line, results are slightly degraded with a rank-1 performance of 0.85. On the other hand, by increasing σ_θ^2 to a relatively large number such as 1000, the orientation attribute has little importance in the distance measurements due to inverse of Σ in (4). As a result, the rank-1 performance dropped to 0.19, which indicates that the information provided by the orientation attribute is significant.

3.1.4. Time complexity

The time necessary to classify a latent fingerprint using the NN path of the algorithm in Fig. 1 is dominated by the set distance calculation. The particles in PSO are searching for the registration that minimizes the LTS-HD measure. A typical swarm of 300 particles searching a tenprint for 150 iterations requires approximately 5 s to settle on a global minima as illustrated in Fig. 4 using an Intel Core i7-920. A query of the 258 tenprints of the SD27

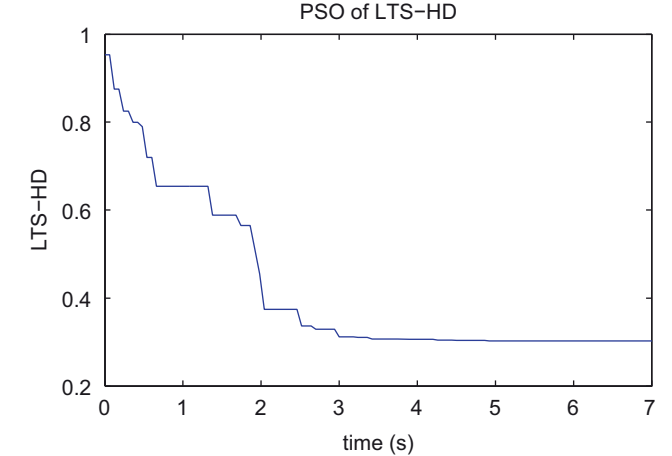


Fig. 4. Typical attributed point patterns in the latent fingerprint experiment contained 20 points in the latent image and 100 points in the tenprint. Calculating the minimized LTS-HD takes approximately 5 s.

database required approximately $258 \times 5 = 1290$ s; however, we accomplished the query in 5 s using 258 cores of the Ohio Supercomputer Center's Opteron Cluster in parallel.

3.1.5. Comparison to prior work

Matching partial fingerprints is a challenging problem with a significant degradation in performance as partial match area approaches 10% [28]. Few studies have been published using SD27. Recently, Feng and Jain [29] reported an accuracy of 73.3% against a background database containing 10,248 images. Jain et al. [30] reported an accuracy of 79.5% with SD27 against a background database containing 2258 images; their method ranks the correct tenprint among the top 20 closest images in 93.4% of cases.

Our results in Section 3.1.3 reported rank-1 and rank-20 classification performances of 71% and 88%, respectively; also, the background database was smaller, containing only the 258 tenprints in the SD27 database. Clearly, the two prior studies [29,30] showed superior results. However, the prior studies were finely tuned to fingerprint matching and used unspecified algorithms to extract additional minutiae attributes. As shown in Section 3.1.3, we achieved a dramatic improvement in classification performance by adding the minutiae direction field to the location attributes. Including additional minutiae features to our attributed point patterns, such as those used in the Jain and Feng studies, may be a promising future study.

3.2. Vehicles in circular synthetic aperture radar

The purpose of this section is to test the hypothesis that X-band radar with only 640 MHz bandwidth (20 cm resolution) operating in circular SAR mode can reliably classify civilian passenger vehicles. The classifier must overcome the spatially variant behavior of radar signatures illustrated in Fig. 6. Numerous previous studies have considered large military vehicles [31]; only two preliminary presentations [15,16] have addressed passenger vehicles. In [15], SAR data from an airborne sensor [32] was used to classify vehicles that were restricted to the scene center.

3.2.1. Generating a circular SAR dataset

A circular SAR generates a set of data called a phase history from a discrete set of radar pulses as the aircraft orbits a scene of interest. Using a physical optics electromagnetic scattering prediction code [33], we generated a phase history for 10 civilian vehicles (Table 1). The vehicle facet models represent a variety of small, mid, and large size civilian vehicles from the late 1990s to early 2000s.

The left part of Fig. 5 shows an example vehicle position V relative to the illuminated patch center or origin O and radar R . The radar, along with its ground projection R_v , orbit the origin in a circular path. The angle of elevation from a vehicle to the radar varies throughout the orbit, except for a vehicle at the origin. For our experiments, we assume the radar is orbiting with an elevation of 45° with respect to O . Furthermore, we assume the terrain is flat asphalt across the patch, resulting in elevation angles between 35° and 59° .

To generate imagery from the phase history data, we used backprojection [34,35] over a 5° aperture and generated 360 images around the SAR orbit with an 80% overlap. Fig. 6(a), (b), (e), (f), (i), and (j) show example images for v_4 , v_8 , and v_9 , where all 360 images are added to give a 360° representation of a vehicle. When generating 2D SAR imagery of a vehicle on asphalt, it is typically possible to visualize an inner and outer ring of scattering. The inner ring is generated by radar echoes that experience a two-bounce path between the asphalt and the side of the vehicle; thus, the inner ring represents time-of-flight to the base outline of the vehicle [36]. In contrast, the outer ring arises from radar echoes reflected by elevated portions of the vehicle, such as the roof line. These elevated features project onto the image in a direction orthogonal to the radar line of sight—an effect known as layover [37]. The polarization feature, v , encodes even versus odd bounce echoes [38–40].

Depending upon the pose and location of the vehicle within the scene, scattering features may migrate or not persist, and the elevated features will exhibit different layover as a function of elevation angle. Thus the same vehicle in two different locations

Table 1

Vehicles identified by a number in experiments.

Number	Model
1	Camry
2	Civic
3	Jeep93
4	Jeep99
5	Maxima
6	MPV
7	Mitsubishi
8	Sentra
9	Avalon
10	Tacoma

For example, the Camry may be referred as 1 or v_1 .

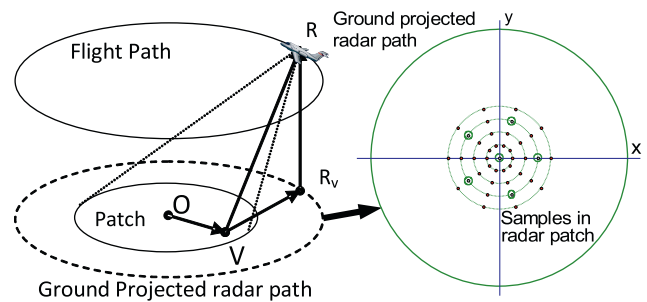


Fig. 5. As a radar R orbits a scene with center O , a vehicle V provides scattering information to the collected phase history. The dataset contains simulated information for the vehicle located at points on the right. Circled points are used for training, while the others are used for classification.

can appear significantly different, as shown in the first two columns of Fig. 6. The first column shows imagery of the vehicle centered in the scene, while the second column shows the vehicle offset along the x -axis by 0.4 times the flight path radius with a 108° pose rotation. Fig. 6(m) and (n) show the position of the vehicles within the scene.

Based on the right half of Fig. 5, we generated 50 sets of images for each of the 10 vehicle classes in Table 1. There are 10 36° pose rotations at the center and 10 locations on each of the four concentric rings about the center. Each vehicle location $v = \|v\|e^{j\theta_v}$ is represented by the pair (β, θ_v) , where $\beta \in \{0.0, 0.1, 0.2, 0.3, 0.4\}$ is the ratio $\beta = \|v\|/\|r_v\|$. The resulting database contains 500 sets of images. Each set of images contains 360 5° subaperture images with 80% overlap. The six circled locations in Fig. 5 are set aside as training samples. Thus, samples in the set $\{(0.0, 0^\circ), (0.3, 0^\circ), (0.3, 72^\circ), (0.3, 144^\circ), (0.3, 216^\circ), (0.3, 288^\circ)\}$ are used for training, while the remaining 44 locations are used as classification samples.

The first step in applying the algorithm shown in Fig. 1 is to process the SAR imagery into an attributed point pattern. The high-frequency scattering response of an object is well approximated as a sum of scattering centers [41], and it is possible to discriminate amongst various objects using an unordered set of feature points [42–46,15,16]. These attributed scattering centers or feature points can include location, amplitude, polarization, and a variety of other attributes [47]. Although radar bandwidth limits the ability to distinguish point sets from two vehicles observed from a given viewing angle [48], the fusion of a diversity of vehicle aspects can greatly enhance discrimination [49–51].

For each image in each set, we implemented a simple peak extractor to approximate scattering center locations. Each scattering center is represented as a vector containing the x and y location, the center azimuth, θ , of the associated imaging aperture, the amplitude, A , of the peak, and an even/odd bounce bit v to encode polarization [38–40,16]. Thus each point in an image is represented by

$$\mathbf{q} = (x, y, \theta, A, v). \quad (18)$$

A vehicle sample is represented by a set

$$Q = \{\mathbf{q}_1, \dots, \mathbf{q}_n\} \quad (19)$$

containing all of the attributed scattering centers in the collection of 360 subaperture images. The last two columns of Fig. 6 provide quiver plots of the location and azimuth information that is derived from the corresponding imagery in the first two columns (the amplitude and bounce attributes are not displayed).

3.2.2. Setting the set distance parameters

To measure the set distances, we apply the LTS-HD based set distance as described in (3). This requires defining a

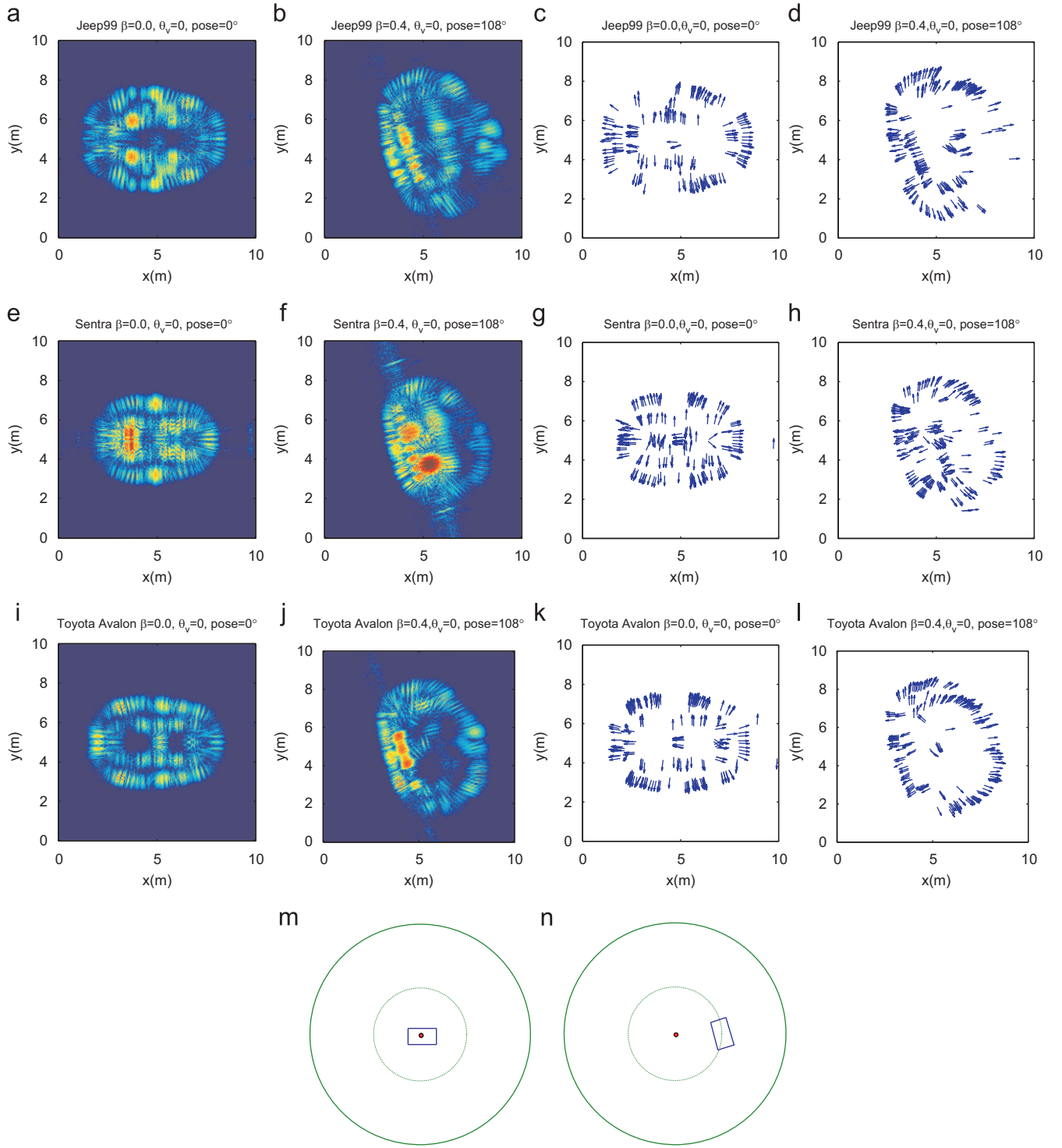


Fig. 6. The left two columns show 360° of SAR imagery for three sample vehicles. For the first column the vehicles are centered in the scene as shown in (m), while the vehicles are offset in the second column as shown in (n). The third and fourth columns show extracted scattering center locations that are attributed with an azimuth attribute. The arrows point in the azimuth direction.

transformation T , a covariance matrix Σ , and a subset cardinality K . First, the transformation is defined by

$$T_i \begin{pmatrix} q_{i_x} \\ q_{i_y} \\ q_{i_\theta} \\ q_{i_A} \\ q_{i_v} \end{pmatrix} = \begin{bmatrix} \begin{bmatrix} \cos\psi & -\sin\psi \\ \sin\psi & \cos\psi \end{bmatrix} \begin{bmatrix} q_{i_x} \\ q_{i_y} \end{bmatrix} + \begin{bmatrix} t_x \\ t_y \end{bmatrix} \\ \text{mod}(q_{i_\theta} + \psi, 2\pi) \\ q_{i_A} \\ q_{i_v} \end{bmatrix}. \quad (20)$$

In SAR, the image scale is known and is independent of range. Thus, it is only necessary to search over rigid transformations with the translations t_x and t_y and the pose rotation ψ . The azimuth attribute θ is transformed directly with the pose rotation, while the amplitude A and even/odd-bounce bit v are not transformed.

To design Σ in the Mahalanobis distance, we chose to populate only the main diagonal for simplicity. Our strategy begins by creating rough estimates for the measurement error variances of

the five attributes. Suppose that we are 95% confident that our scattering center peak locations x and y are within two pixels of their true locations (i.e. within a 12 cm). Thus,

$$2 = 1.98\sigma_x \Rightarrow \sigma_x^2 = \sigma_y^2 \approx 1. \quad (21)$$

Now, suppose that the azimuth attribute for each peak is uniformly distributed over the 5° aperture; hence

$$\sigma_\theta^2 = \frac{(b-a)^2}{12} = \frac{5^2}{12} \approx 2. \quad (22)$$

For the amplitude attribute, log-normal and quarter-power normal models have been widely adopted for nonclutter peaks [52]. Under the log-normal assumption, suppose that with 95% confidence, the amplitude measurement is accurate within 5 dB (zero dB is the maximum peak in the data set); thus

$$5 = 1.98\sigma_A \Rightarrow \sigma_A^2 \approx 2.5^2 = 6.25. \quad (23)$$

Lastly, suppose that the even/odd bounce bit v is correct with probability $\phi = 0.95$; thus

$$\sigma_v^2 = \phi(1-\phi) = 0.95(1-0.95) = 0.05. \quad (24)$$

Next, we selected the training samples for two similar vehicles, v1 and v5, to test class separation based on the estimated Σ . Then, we applied MDS in \mathbb{R}^3 to visualize the class separation. By individually tuning the five variance terms, it was possible to improve class separation; however, the initial estimates were close to the tuned selections.

The last parameter is the subset cardinality parameter K . Using the method in (5), we selected $r=0.7$, applied to the smallest set of points in the training set. This allowed for the set distance to ignore at least 30% of the points in calculating the LTS-HD between two point patterns.

3.2.3. Circular SAR classification results

Using the experiment described in Section 3.2.1 with set distance parameters described in Section 3.2.2, we applied the NN classifier of Fig. 1, which finds the minimum set distance from each query to the 60 training samples. Table 2(a) shows the classification result as a confusion matrix. Each row of the matrix represents the actual vehicle in the 440 query samples, while the columns represent the classification results. An ideal confusion matrix would contain all 44s on the diagonal and zeros elsewhere. Dividing the trace of the confusion matrix by 440 quantifies performance as a probability of correct identification, P_{id} . The result is a classification performance of $P_{id}=0.977$. With only one training sample at the origin of Fig. 5, as shown in Table 2(b), the performance drops to $P_{id}=0.918$.

Next, we investigated visualization, analysis, and alternative classification using an MDS/LMDS embedding, starting with a visualization. Some pairs of vehicle classes were easily separated in an \mathbb{R}^2 embedding. Fig. 7 shows an example MDS/LMDS embedding of the Sentra (v8) and the Avalon (v9); notice that these vehicles were also used in the example imagery of Fig. 6. Applying the minimized LTS-HD to all of the pairings of the six training samples for each class generated a 12×12 EDM of set distances. Next, by solving the eigendecomposition from Eq. (11), the red pluses in Fig. 7(a) and (b) along with the green asterisks represent the MDS embedding for the Sentra and Avalon, respectively. Based on the six training samples, now in a Euclidean space, a support vector machine with a linear basis easily separates the classes as shown with a line using the circled support vectors. Using LMDS from Section 2.3, Fig. 7(a) shows the embedding and proper classification of the 44 Sentry samples with pink pluses. Likewise, Fig. 7(b) shows the embedding and proper classification of the 44 Avalon samples with blue asterisks.

Table 2

These confusion matrices show actual vs. classified results for 10 vehicles using a NN classifier: (a) has 6 training samples per class, while (b) uses only one training sample per class.

(a) NN, T6, $P_{id}=0.977$										
	1	2	3	4	5	6	7	8	9	10
1	44	0	0	0	0	0	0	0	0	0
2	0	43	0	0	0	0	1	0	0	0
3	0	0	36	7	0	1	0	0	0	0
4	0	0	0	43	1	0	0	0	0	0
5	0	0	0	0	44	0	0	0	0	0
6	0	0	0	0	0	44	0	0	0	0
7	0	0	0	0	0	0	44	0	0	0
8	0	0	0	0	0	0	0	44	0	0
9	0	0	0	0	0	0	0	0	44	0
10	0	0	0	0	0	0	0	0	0	44

(b) NN, T1, $P_{id}=0.918$										
	1	2	3	4	5	6	7	8	9	10
1	39	0	0	0	4	0	0	1	0	0
2	0	43	1	0	0	0	0	0	0	0
3	0	2	31	1	4	0	0	0	6	0
4	0	1	0	43	0	0	0	0	0	0
5	0	0	0	0	41	0	1	2	0	0
6	0	0	0	1	1	41	0	0	1	0
7	0	2	0	0	0	0	42	0	0	0
8	0	0	0	0	4	0	0	40	0	0
9	0	2	0	0	0	0	0	2	40	0
10	0	0	0	0	0	0	0	0	0	44

Based on the example in Fig. 7, the LTS-HD, although not a true distance metric, was able to separate two classes in an \mathbb{R}^2 embedding with perfect classification results. In a more general sense, we can look at the eigenvalues of the Schoenberg augmented EDMs to see how well the selected set distance adheres to the triangle inequality. Fig. 8 describes the eigenvalues for the SAR application. The plot in Fig. 8(a) shows the eigenvalues for the v1 to v3 comparison, which had the best set of eigenvalues for all pairings in the dataset. It has only one small negative eigenvalue, and the embedding is nearly perfect in \mathbb{R}^9 . One of the worst pairings is the pattern shown in Fig. 8(b) for v4 to v8, where the first seven dominant eigenvalues are positive. In general, for the entire set of data on average, as shown in Figs. 8(c) and (d), most of the information is stored in the dominant eigenvalues, and few small eigenvalues are negative.

Next, we applied MDS to the 45 vehicle pairings in the 10 class problem. For each pairing, we investigated the performance of a binary decision tree using nearest neighbor, LDA, linear SVM, and radial basis function (RBF) SVM classifiers. Each decision was similar to the plots described in Fig. 7. By using LMDS, each of the 440 classification samples is embedded and classified using nine binary comparisons in the classification tree. For example, a sample is classified in each of the pairings (v1,v2), (v3,v4), (v5,v6), (v7,v8), and (v9,v10), thus leaving five winners. Subsequently, we continue classifying pairs until a winner is selected. The 10 class problem requires four levels of decisions (10,5,3,2) for nine total decisions (5+2+1+1).

Fig. 9 displays the results for a variety of classifiers and embedding dimensions. There were at least seven positive eigenvalues for each MDS embedding of the training samples; thus, we tested the classifiers in each of the first seven dimensions. The RBF-SVM in \mathbb{R}^4 was the best performing classifier with $P_{id}=0.941$, as highlighted with the confusion matrix in Table 3.

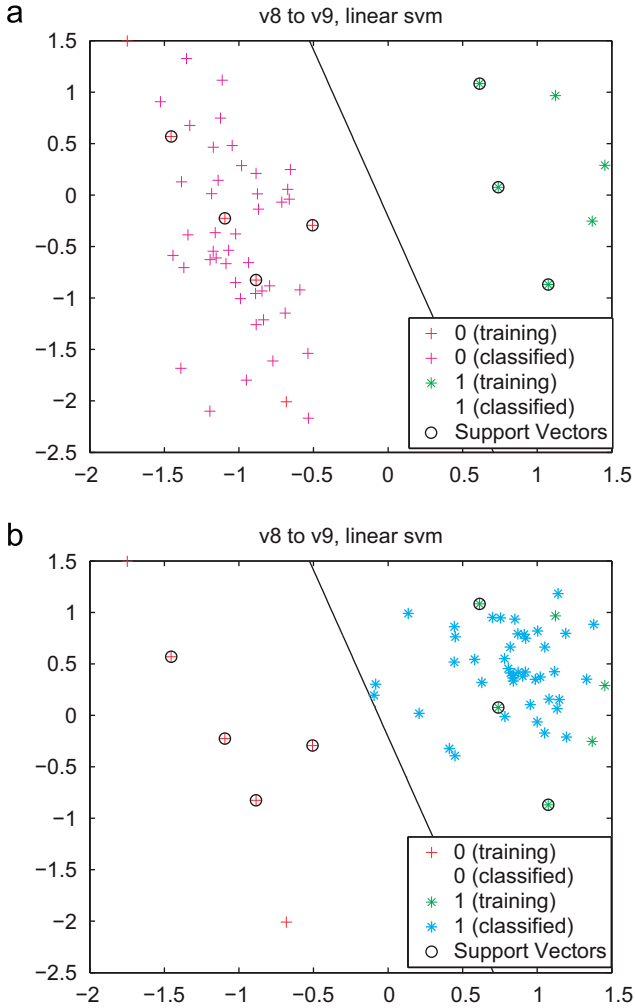


Fig. 7. MDS enables visualization of the point patterns as vectors in \mathbb{R}^2 . The plot in (a) shows v8 samples properly classified, while (b) shows v9 samples properly classified.

We note two observations from the confusion matrices. First, in the NN classifier of Table 2(a), most of the classification errors were caused when distinguishing the two models of Jeep in v3 and v4. Second, the SVM classifier in \mathbb{R}^4 resolves confusion between the Jeep models, but causes several vehicles to be misclassified as a Civic, v2.

These results show that a LTS-HD minimized over rigid transformations can classify a 10 class circular SAR application in a large scene with greater than 97% accuracy using six scattered templates. Even using a single training sample, the performance is greater than 91%. The MDS/LMDS processing did not improve performance in this case; however, it did provide a tool for visualizing samples for class separation and analyzing the minimized LTS-HD via the eigenvalues generated during the embedding process.

3.2.4. Time complexity

The time required to classify a query vehicle from the circular SAR experiment is dominated by the time required to solve the nonconvex PSO optimization of the LTS-HD. Fig. 10 shows the progression of a typical minimization between a pair of 200 point patterns. Although, efficient selection of stopping criteria for a PSO is an open problem [24], based on training data, we determined that 100 particles for 100 iterations provides stable results. Each minimized LTS-HD was calculated in approximately

15 s; a nearest neighbor test on the 60 training samples in the SAR database required 15 min, when single threaded. Both the PSO and nearest neighbor tests are highly parallelizable for real time performance.

3.2.5. Comparison to MSE classifier

There exist no prior studies for object classification using circular SAR or for radar identification of civilian vehicles. To provide a benchmark comparison, we use the mean squared error (MSE) classifier. MSE provides a generalized likelihood ratio test for translated patterns in additive white Gaussian noise, and is therefore widely used; but, MSE is known to be brittle in the presence of occlusion, clutter, and other nonideal conditions [53–55]. We compared the minimized LTS-HD classifier to the MSE classifier as applied to the data set of Section 3.2.1. Whereas the LTS-HD based classifier compares sets of vectors (attributed point patterns), the MSE classifier compares images like those in Fig. 6a.

When comparing a query image to a database image, the minimized LTS-HD classifier uses a particle swarm optimization to find the registration that minimizes the distance over rigid transformations (both rotation and translations in a plane). On the other hand, the MSE classifier uses an FFT based method to align the images in translation prior to calculating the Euclidean distance between high dimensional vectors of columnwise ordered image pixels. We minimize the MSE distance over 72 possible rotations with 5° spacing. The 60 vehicles of the point pattern database required 240 kB of storage, while the database images for the MSE method required 15.7 MB.

The results showed that the MSE classifier had only two misclassifications of the 440 samples for a 99.6% performance; this compares to the LTS-HD method performance of 97.7% from Table 3. Classification time for the MSE was also faster, requiring 6.1 s to generate a distance between the query and each training sample (using MATLAB on the Intel Core i7-920) versus 15 s for the LTS-HD method. These results for the MSE based classifier, are impressive; however, under partial occlusions of the query, the LTS-HD shows a strong performance advantage.

Suppose that half of data from the query samples is occluded [56]; i.e., the line of sight to the vehicles was blocked for 180° of the circular aperture. The LTS-HD based classifier appropriately registers the available data within the training database images, while the MSE based classifier fails to register the images properly. We ran a comparative experiment on row five of Table 3, and the results are shown in Table 4. The MSE classifier performs at 15.9% compared to 86.4% for the LTS-HD classifier. Furthermore, with fewer points in the query sets, the LTS-HD classifier query times are reduced by approximately 50%.

4. Discussion

In this paper, we described a procedure for classifying sets of attributed point patterns, where each point pattern is a collection of feature vectors. Registration of point patterns in the translation-variant case is obtained using a version of the Hausdorff distance, called the LTS-HD, that is minimized over a set of transformations. The minimized LTS-HD was termed the set distance. As a novel contribution to the point pattern registration and set distance calculation, we chose a Mahalanobis distance to calculate distances between individual points. This allowed for a principled fusion of feature attributes using the normalization provided by the error covariance matrix. The minimized LTS-HD, when comparing a query to a database, was used in a nearest neighbor classifier.

For the case of multiple training samples per class, we described an implementation of multidimensional scaling to

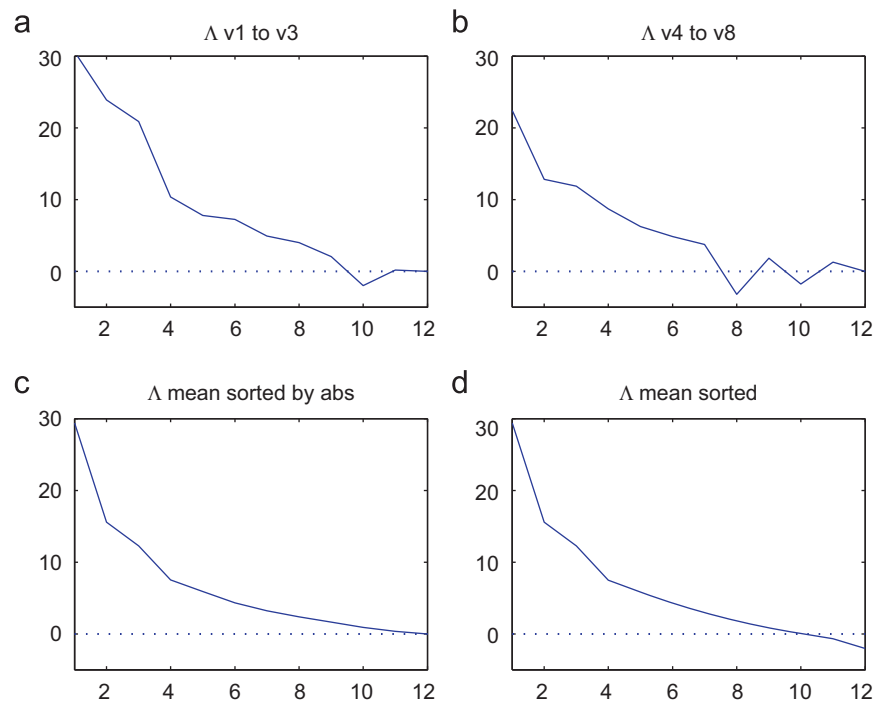


Fig. 8. Eigenvalues for the Schoenberg augmented Euclidean distance matrices are displayed. (a) and (b) show representative examples, while (c) and (d) show the average trends for the dataset. There are several large positive eigenvalues and the few negative ones are small.

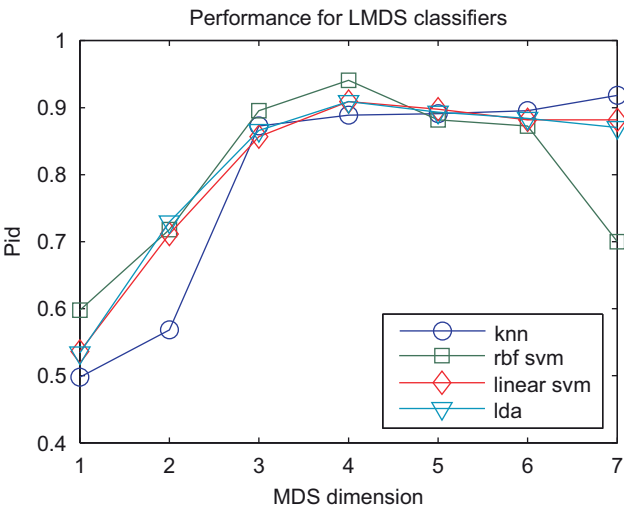


Fig. 9. The probability of correct classification for several classifiers is displayed versus embedding dimension. Generally, performance peaks around \mathbb{R}^4 with similar performance for all four classifiers.

embed sets of point patterns in a Euclidean space. The MDS algorithm requires a matrix of pairwise distances between samples; in our application, we used the minimized LTS-HD based pseudo-distance. After embedding point patterns within the Euclidean space, it was possible to visualize the class separation in dimensions of 3D or less. In addition, the eigenvalues that were generated as part of the MDS process were useful in determining the suitability of the pseudo-metric as a distance measure. It was also possible to train standard classifiers such as LDA or SVM, and embed query samples in the same Euclidean space using LMDS.

The proposed classification strategy was applied to yield the first reported radar classification results for civilian passenger vehicles. The use of attributed point sets provided high-confidence

Table 3
Confusion matrix showing actual vs. classified results for 10 vehicles after applying MDS/LMDS with an RBF-SVM classifier.

RBF SVM, \mathbb{R}^4 , $P_{id}=0.941$										
	1	2	3	4	5	6	7	8	9	10
1	42	0	0	0	2	0	0	0	0	0
2	1	43	0	0	0	0	0	0	0	0
3	0	0	44	0	0	0	0	0	0	0
4	0	0	0	44	0	0	0	0	0	0
5	0	0	0	0	42	0	0	2	0	0
6	0	6	0	4	0	34	0	0	0	0
7	1	6	0	0	0	0	37	0	0	0
8	0	1	0	0	0	0	1	42	0	0
9	0	2	0	0	0	0	0	0	42	0
10	0	0	0	0	0	0	0	0	0	44

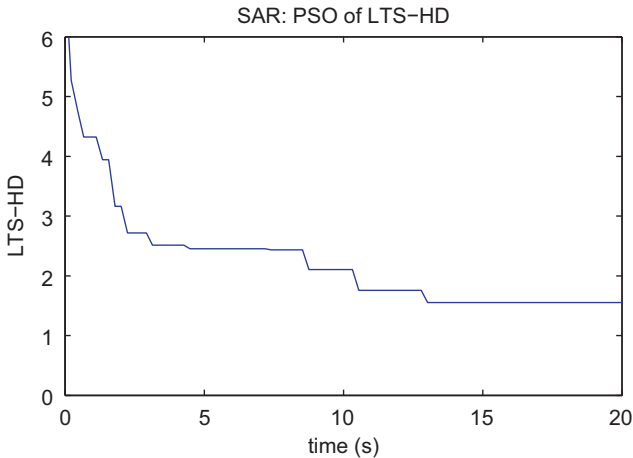


Fig. 10. Typical attributed point patterns in the SAR experiment contained on the order of 200 points per set, and calculating the minimized LTS-HD, using a particle swarm optimization, required approximately 15 s.

Table 4

When classifying the Maxima using 180° of aspect, the MSE classifier performs poorly (a), while the minimized LTS-HD shows a relatively good performance (b).

(a) MSE, 180°, $P_{id}=0.159$										
	1	2	3	4	5	6	7	8	9	10
5	10	9	0	0	7	0	18	0	0	0
(b) LTS-HD, 180°, $P_{id}=0.864$										
	1	2	3	4	5	6	7	8	9	10
5	0	3	0	0	38	0	0	1	2	0

classification with robustness to obscuration. The use of a Mahalanobis point distance allowed principled scaling of attributes that enhance class separability. In addition, a fingerprint application extended minutiae registration results from [11] to demonstrate the generic applicability of the proposed classification approach using attributed point sets.

Acknowledgments

This work was supported in part by an allocation of computing time from the Ohio Supercomputer Center. This material is based upon work supported by the Air Force Research Laboratory under Award FA8650-07-D-1220 and by the Air Force Office of Scientific Research under Award FA9550-06-1-0324. Any opinions, findings, conclusions or recommendations expressed in this publication are those of the authors and do not necessarily reflect the views of the US Air Force. The US Government is authorized to reproduce and distribute reprints for Governmental purposes notwithstanding any copyright notation thereon.

References

- [1] D. Maltoni, D. Maio, A. Jain, S. Prabhakar, *Handbook of Fingerprint Recognition*, Springer, London, 2009.
- [2] M. Fernandez, G. Valiente, A graph distance metric combining maximum common subgraph and minimum common supergraph, *Pattern Recognition Letters* 22 (2000) 753–758.
- [3] B. Luo, E. Hancock, Structural graph matching using the EM algorithm and singular value decomposition, *IEEE Trans. Pattern Anal. Mach. Intell.* 23 (10) (2001) 1120–1136.
- [4] M. Carcassoni, E.R. Hancock, Spectral correspondence for point pattern matching, *Pattern Recognition* 36 (2003) 193–204.
- [5] M. Carcassoni, E.R. Hancock, Correspondence matching with modal clusters, *IEEE Trans. Pattern Anal. Mach. Intell.* 25 (12) (2003) 1609–1615.
- [6] K.S. Arun, T.S. Huang, S.D. Blosteing, Least-squares fitting of two 3-D point sets, *IEEE Trans. Pattern Anal. Mach. Intell.* 9 (5) (1987) 592–606.
- [7] S. Umeyama, Least-squares estimation of transformation parameters between point patterns, *IEEE Trans. Pattern Anal. Mach. Intell.* 13 (4) (1991) 376–380.
- [8] P.J. Besl, N.D. McKay, A method for registration of 3-D shapes, *IEEE Trans. Pattern Anal. Mach. Intell.* 14 (2) (1992) 239–256.
- [9] Y. Liu, Improving icp with easy implementation for free-form surface matching, *Pattern Recognition* 37 (2004) 211–226.
- [10] D.P. Huttenlocher, G.A. Klanderman, W.J. Rucklidge, Comparing images using the Hausdorff distance, *IEEE Trans. Pattern Anal. Mach. Intell.* 15 (1993) 850–863.
- [11] P.-Y. Yin, Particle swarm optimization for point pattern matching, *J. Vis. Commun. Image R.* 17 (2006) 143–162.
- [12] K. Sturtz, G. Arnold, M. Ferrara, DC optimization modeling for shape-based recognition, in: E.G. Zelnio, F.D. Garber (Eds.), *Algorithms for Synthetic Aperture Radar Imagery XVI*, Proceedings of the SPIE, vol. 7337, 2009, p. 733700.
- [13] M.P. Dubuisson, A.K. Jain, A modified Hausdorff distance for object matching, in: *Proceedings of the 12th IAPR International Conference on Pattern Recognition*, Conference A: Computer Vision & Image Processing, 9–13 October 1994, pp. 566–568.
- [14] C. Zhao, W. Shi, Y. Deng, A new hausdorff distance for image matching, *Pattern Recognition Letters* 26 (2005) 581–586.
- [15] K.E. Dungan, L.C. Potter, J. Blackaby, J. Nehrbass, Discrimination of civilian vehicles using wide-angle SAR, in: E.G. Zelnio, F.D. Garber (Eds.), *Algorithms for Synthetic Aperture Radar Imagery XV*, Proceedings of the SPIE, vol. 6970, 2008, p. 69700Z.
- [16] K.E. Dungan, L.C. Potter, Classifying civilian vehicles using a wide-field circular SAR, in: E.G. Zelnio, F.D. Garber (Eds.), *Algorithms for Synthetic Aperture Radar Imagery XVI*, Proceedings of the SPIE, vol. 7337, 2009, p. 73370R.
- [17] V. de Silva, J.B. Tenenbaum, Sparse multidimensional scaling using landmark points <http://pages.pomona.edu/~vds04747/public/papers/landmarks.pdf>, 2004.
- [18] F. Hausdorff, *Grundzüge der Mengenlehre*, Veit and Company, Leipzig, 1914.
- [19] D.-G. Sim, O.-K. Kwon, R.-H. Park, Object matching algorithms using robust Hausdorff distance measures, *IEEE Trans. Image Process.* 8 (3) (1999) 425–429.
- [20] W. Rucklidge, *Efficient Visual Recognition Using the Hausdorff Distance*, Springer, Berlin, 1996.
- [21] P.C. Mahalanobis, On the generalised distance in statistics, *Proc. Natl. Inst. Sci. India* 2 (1) (1936) 49–55.
- [22] D.M. Mount, N.S. Netanyahu, J.L. Moigne, Improved algorithms for robust point pattern matching and applications to image registration, in: *Proceedings of the 14th Annual Symposium on Computational Geometry*, Proceedings of the ACM, 1998, pp. 155–164.
- [23] M. Clerc, J. Kennedy, The particle swarm—explosion, stability, and convergence in a multidimensional complex space, *IEEE Trans. Evol. Comput.* 6 (2002) 58–73.
- [24] N.M. Kwok, Q.P. Ha, D.K. Liu, G. Fang, K.C. Tan, Efficient particle swarm optimization: a termination condition based on the decision-making approach, in: *IEEE Congress on Evolutionary Computation*, Singapore, 2007, pp. 3353–3360.
- [25] L.C. Potter, D. Chiang, Distance matrices and modified cyclic projections for molecular conformation, *IEEE International Conference on Acoustics, Speech, and Signal Processing*, vol. 4, 1992, pp. 173–176.
- [26] I.J. Schoenberg, Remarks to Maurice Frechet's article 'Sur la definition axiomatique d'une classe d'espaces vectoriels distances applicables vectoriellement sur l'espace de Hilbert', *Ann. Math.* 36 (1935) 724–732.
- [27] M.D. Garriss, R.M. McCabe, NIST special database 27 fingerprint minutiae from latent and matching tenprint images, Technical Report NISTIR 6534, National Institute of Standards and Technology, 2000.
- [28] T.-Y. Jea, V. Govindaraju, A minutia-based partial fingerprint recognition system, *Pattern Recognition* 38 (2005) 1672–1684.
- [29] F. Jianjiang, A.K. Jain, Filtering large fingerprint database for latent matching, in: *19th International Conference on Pattern Recognition*, Tampa, FL, 2008, pp. 1–4.
- [30] A.K. Jain, J. Feng, A. Nagar, K. Nandakumar, On matching latent fingerprints, in: *IEEE Computer Society Conference on Computer Vision and Pattern Recognition Workshops*, Anchorage, AK, 2008, pp. 1–8.
- [31] L.M. Novak, G.J. Owirka, C.M. Netishen, Performance of a high-resolution polarimetric SAR automatic target recognition system, *Lincoln Lab. J.* 6 (1) (1993) 11–23.
- [32] C.H. Casteel Jr., L.A. Gorham, M.J. Minardi, S.M. Scarborough, K.D. Naidu, U.K. Majumder, A challenge problem for 2D/3D imaging of targets from a volumetric data set in an urban environment, in: E.G. Zelnio, F.D. Garber (Eds.), *Algorithms for Synthetic Aperture Radar Imagery XIV*, Proceedings of the SPIE, vol. 6568, 2007, p. 65680D.
- [33] K.E. Dungan, C. Austin, J. Nehrbass, L.C. Potter, Civilian vehicle radar data domes, in: E.G. Zelnio, F.D. Garber (Eds.), *Algorithms for Synthetic Aperture Radar Imagery XVII*, Proceedings of the SPIE, vol. 7699, 2010.
- [34] L.A. Gorham, U.K. Majumder, P. Buxa, M.J. Backues, A.C. Lindgren, Implementation and analysis of a fast backprojection algorithm, in: E.G. Zelnio, F.D. Garber (Eds.), *Algorithms for Synthetic Aperture Radar Imagery XIII*, Proceedings of the SPIE, vol. 6237, Orlando, 2006, p. 62370G.
- [35] D.E. Wahl, D.A. Yocky, C.V. Jakowatz Jr., An implementation of a fast backprojection image formation algorithm for spotlight-mode sar, in: E.G. Zelnio, F.D. Garber (Eds.), *Algorithms for Synthetic Aperture Radar Imagery XV*, Proceedings of the SPIE, vol. 6970, Orlando, 2008, p. 69700H.
- [36] K.E. Dungan, L.C. Potter, Three-dimensional imaging of vehicles with wide-angle synthetic aperture radar, *IEEE Trans. Aerosp. Electron. Syst.*, <http://www.ece.osu.edu/~potter/papers/Dungan_IEEEAES08_preprint.pdf>.
- [37] C.V. Jakowatz Jr., D.E. Wahl, P.H. Eichel, D.C. Ghiglia, P.A. Thompson, *Spotlight-mode Synthetic Aperture Radar: A Signal Processing Approach*, Kluwer Academic Publishers, Norwell, MA, 1996.
- [38] D. Giulio, Polarization diversity in radars, *Proceedings of the IEEE* 74 (1986) 245–269.
- [39] L.M. Novak, M.C. Burl, W.W. Irving, Optimal polarimetric processing for enhanced target detection, *IEEE Trans. Aerosp. Electron. Syst.* 29 (1993) 234–244.
- [40] E. Ertin, L.C. Potter, Polarimetric classification of scattering centers using Mary Bayesian decision rules, *IEEE Trans. Aerosp. Electron. Syst.* 36 (3) (2000) 738–749. doi:10.1109/7.869492.
- [41] J.B. Keller, Geometrical theory of diffraction, *J. Opt. Soc. Am.* 52 (3) (1962) 116–130.
- [42] G.J. Ettinger, G.A. Klanderman, W.M. Wells, W.E.L. Grimson, Probabilistic optimization approach to SAR feature matching, in: E.G. Zelnio, R.J. Douglass (Eds.), *Algorithms for Synthetic Aperture Radar Imagery III*, Proceedings of the SPIE, vol. 2757, Orlando, 1996, pp. 318–329.

- [43] H.-C. Chiang, R.L. Moses, L.C. Potter, Model-based classification of radar images, *IEEE Trans. Inf. Theory* 46 (5) (2000) 1842–1854.
- [44] H.-C. Chiang, R.L. Moses, L.C. Potter, Model-based Bayesian feature matching with application to synthetic aperture radar target recognition, *Pattern Recognition* 34 (8) (2001) 1539–1553.
- [45] B. Bhanu, G. Jones III, Increasing the discrimination of synthetic aperture radar recognition models, *Opt. Eng.* 41 (12) (2002) 3298–3306.
- [46] B. Bhanu, G. Jones III, R. Wang, Composite class models for SAR recognition, in: E.G. Zelnio, F.D. Garber (Eds.), *Algorithms for Synthetic Aperture Radar Imagery X*, Proceedings of the SPIE, vol. 5095, Orlando, 2003, pp. 284–291.
- [47] L.C. Potter, R.L. Moses, Attributed scattering centers for SAR ATR, *IEEE Trans. Image Process.* 6 (1) (1997) 79–91.
- [48] W.W. Irving, R.B. Washburn, W.E.L. Grimson, Bounding performance of peak-based target detectors, in: E.G. Zelnio (Ed.), *Algorithms for Synthetic Aperture Radar Imagery IV*, Proceedings of the SPIE, vol. 3070, Orlando, 1997, pp. 245–257.
- [49] G.G. Brendel, L.L. Horowitz, Benefits of aspect diversity for SAR ATR: fundamental and experimental results, in: E. G. Zelnio (Ed.), *Algorithms for Synthetic Aperture Radar Imagery VII*, Proceedings of the SPIE, vol. 4053, Orlando, 2000, pp. 567–578.
- [50] G. Ettinger, W. Snyder, Model-based fusion of multi-look SAR for ATR, in: E.G. Zelnio (Ed.), *Algorithms for Synthetic Aperture Radar Imagery IX*, Proceedings of the SPIE, vol. 4727, Orlando, 2002, pp. 277–289.
- [51] B. Bhanu, G. Jones III, Exploiting azimuthal variance of scatterers for multiple look SAR recognition, in: E.G. Zelnio (Ed.), *Algorithms for Synthetic Aperture Radar Imagery IX*, Proceedings of the SPIE, vol. 4727, Orlando, 2002, pp. 290–298.
- [52] M.D. DeVore, J.A. O'Sullivan, Statistical assessment of model fit for synthetic aperture radar data, in: E.G. Zelnio (Ed.), *Algorithms for Synthetic Aperture Radar Imagery VIII*, Proceedings of the SPIE, vol. 4382, Orlando, 2001, pp. 358–366.
- [53] T. Ross, S. Worrel, V. Velten, J. Mossing, M. Bryant, Standard SAR ATR evaluation experiments using the MSTAR public release data set, in: E.G. Zelnio (Ed.), *Algorithms for Synthetic Aperture Radar Imagery V*, Proceedings of the SPIE, vol. 3370, Orlando, 1998, pp. 566–573.
- [54] M.L. Bryant, S.W. Worrell, A.C. Dixon, MSE template size analysis for mstar data, in: E.G. Zelnio (Ed.), *Algorithms for Synthetic Aperture Radar Imagery V*, Proceedings of the SPIE, vol. 3370, Orlando, 1998, pp. 396–405.
- [55] L.M. Novak, G.J. Owirka, W. Brower, Performance of 10- and 20-target MSE classifiers, *IEEE Trans. Aerosp. Electron. Syst.* 36 (4) (2000) 1279–1289.
- [56] T.D. Ross, J.J. Bradley, L.J. Hudson, M.P. O'Connor, SAR ATR—so what's the problem?—an MSTAR perspective, in: E.G. Zelnio (Ed.), *Algorithms for Synthetic Aperture Radar Imagery VI*, Proceedings of the SPIE, vol. 3721, Orlando, 1999, pp. 662–672.

Kerry E. Dungan received his B.S., M.S., and Ph.D. degrees from The Ohio State University, Columbus, in 1994, 1997, and 2010, all in Electrical & Computer Engineering. Kerry worked for Harris Corporation, Lucent Technologies, and Synplicity as a member of Technical Staff and Technical Account Manager in the area of embedded systems. He is currently a Postdoctoral Researcher at Ohio State.

Lee C. Potter received the B.E. degree from Vanderbilt University, Nashville, TN, and the M.S. and Ph.D. degrees from the University of Illinois at Urbana-Champaign, all in Electrical Engineering. Since 1991, he has been with the Department of Electrical & Computer Engineering, The Ohio State University, Columbus, where he is currently an Associate Professor. Dr. Potter is recipient of the 1993 MacQuigg Award for Outstanding Teaching.